Ultramicroscopy 132 (2013) 143–151

Contents lists available at ScienceDirect

Ultramicroscopy

journal homepage: www.elsevier.com/locate/ultramic

Mapping energetics of atom probe evaporation events through first principles calculations

Joaquín Peralta *, Scott R. Broderick, Krishna Rajan **

Department of Materials Science and Engineering and Institute for Combinatorial Discovery, Iowa State University, 2220 Hoover Hall, Iowa State University, Ames, IA 50011-2230, United States

ARTICLE INFO

Available online 28 February 2013

Keywords:
Atom probe tomography
Simulations
Ab initio
Field evaporation
Evaporation maps

ABSTRACT

The purpose of this work is to use atomistic modeling to determine accurate inputs into the atom probe tomography (APT) reconstruction process. One of these inputs is evaporation field; however, a challenge occurs because single ions and dimers have different evaporation fields. We have calculated the evaporation field of Al and Sc ions and Al–Al and Al–Sc dimers from an $L1_2$-Al_3Sc surface using ab initio calculations and with a high electric field applied to the surface. The evaporation field is defined as the electric field at which the energy barrier size is calculated as zero, corresponding to the minimum field that atoms from the surface can break their bonds and evaporate from the surface. The evaporation field of the surface atoms are ranked from least to greatest as: Al–Al dimer, Al ion, Sc ion, and Al–Sc dimer. The first principles results were compared with experimental data in the form of an ion evaporation map, which maps multi-ion evaporations. From the ion evaporation map of $L1_2$-Al_3Sc, we extract relative evaporation fields and identify that an Al–Al dimer has a lower evaporation field than an Al–Sc dimer. Additionally, comparatively an Al–Al surface dimer is more likely to evaporate as a dimer, while an Al–Sc surface dimer is more likely to evaporate as single ions. These conclusions from the experiment agree with the ab initio calculations, validating the use of this approach for modeling APT energetics.

1. Introduction

Atom probe tomography provides pico-scale spatial resolution with 3D chemical imaging [1–3]. Since the pioneer work of McMullen [4,5] and Kreuzer et al. [6], many simulations of APT data have been performed on field evaporation using both ab initio [7–9] and empirical techniques [10–14]. These simulations were used to study the effects of electric field on the surface [15,9]. Here we use ab initio simulations, based on density functional theory (DFT), to calculate the critical evaporation field (F_e) of different evaporation events for the purpose of APT data reconstruction [16–20]. An example of a reconstruction algorithm is the Bas protocol [21,17], where the reconstruction spatial points (x,y) are related to the magnification M by $(x,y)=(X_D/M,Y_D/M)$, where X_D and Y_D correspond to APT detector positions. The magnification is represented by $M\propto L/\xi R$, with L the distance between the sample and the detector screen, R is the radius of curvature of the emitter apex, and ξ is the image compression factor. Because $R=V/k_fF_{op}$, we have

$$(x,y)\propto\left(\frac{\xi}{k_fF_{op}},\frac{\xi}{k_fF_{op}}\right) \tag{1}$$

where V is the applied voltage, k_f is the geometrical field factor, and F_{op} is the operational evaporation field actually used in atom probe experiments, and which can be assumed to be less than the critical evaporation field, F_e. For the case of the z component used in this reconstruction algorithm:

$$dz=\frac{\Omega(Lk_fF_{op})^2}{V^2(\eta S_d\xi^2)} \tag{2}$$

where Ω is the atomic volume, S_d is the surface area of the detector, and η is the detector efficiency. Finally the z coordinate of the reconstruction is given by $z=(\sum dz)+dz'$, where $dz'=R-\sqrt{(x^2+y^2)}$. With this, the dependence of z with respect to the operating evaporation field is $z\propto F_{op}^3$. Eqs. (1) and (2) show that, for this model, the value entered for F_{op} is related to the reconstructed spatial coordinates. Therefore, an incorrect value of F_{op} leads to an error in the reconstruction process, with F_{op} highly dependent on the chemistry and crystal structure of the evaporated atoms [22,23]. Moreover, given that the critical field evaporation (F_e) can be assumed bigger than F_{op}, errors in the use of these parameters are likely.

* Corresponding author. Tel.: +1 5152942670.
** Principal corresponding author.
E-mail addresses: jperaltac@gmail.com (J. Peralta), sbroderick@iastate.edu (S.R. Broderick), krajan@iastate.edu (K. Rajan).

0304-3991/$ - see front matter © 2013 Elsevier B.V. All rights reserved.
http://dx.doi.org/10.1016/j.ultramic.2013.02.007

Cases have been shown where certain elements are more likely to evaporate as dimers than others [24,25]. It is this effect that we are assessing by calculating the evaporation field of dimers versus the constituent atoms from the same structure. As described, the evaporation field is used in the reconstruction process, and dimers have different evaporation fields than single atoms. Therefore, even if correct values for single atoms are input into the reconstruction, error is introduced with the dimers because of different evaporation fields. It is the calculation of F_e for dimers that we consider here, and not errors in data collection due to the dimers being incorrectly measured by the detector [26,27].

In order to determine the F_e value by means of ab initio simulations, different approaches have been used [8,23], mostly based on the image-hump model [28,29]. This model proposes the presence of a hump in the energy of the system when an electric field is applied, which disappears when the F_e value is reached. From this model, the activation energy is given by

$$Q = (E_b + I - n\phi) - \sqrt{\frac{-n^3 e^3 F}{4\pi\epsilon_0}} \tag{3}$$

where Q is the activation energy for an ion of charge ne, e is the elementary positive charge, ϵ_0 is the electric constant, E_b corresponds to the binding energy of the neutral atom to the surface, I is the sum of the first n ionization energy, ϕ is the work function, and F is the electric field. This basic image-hump model is purely classical, and neglects the existence of repulsive forces between the evaporating atom and the surface. For many materials, it has been shown that this model predicts a dependence of activation energy on field that disagrees with experiment (see, for example, [30]). However, it has recently been shown [8] that the basic image-hump formula provides a satisfactory empirical description of first-principles calculations for aluminium. The reasons for this are not clear because the physical basis of the two approaches are very different. The basic image-hump formula assumes that charge on the atom is integral and constant as the atom goes over the hump, whereas [8] finds charge on the atom to be non-integral and varying as the atom goes over the hump. Another well-known model is the charge exchange model [31,29] that is considered more applicable than the image-hump; however, it is not easy to work with because it requires explicit knowledge of the atomic and ionic energy–distance curve [32], which is beyond the scope of the present work. Based on this, we propose a numerical approximation based on a variation of the hump model to determine the field evaporation value.

In order to experimentally validate our computational results, the concept of an ion evaporation map is used to investigate multiple-hit events where two objects arrive at the detector close together in time [33]. While the majority of these occurrences are due to two ions evaporated at closely adjacent times, it has been shown [34] that these events also result from dimer evaporations, which may also break-up during flight. These maps however can provide some insight into different evaporation events, including those associated with the evaporation of dimers. The reason for linking ion evaporation maps and ab initio calculations is to compare the counting statistics one observes with ion evaporation maps with the energetic feasibility of those events to occur (as calculated through ab initio).

The relative changes in the ion evaporation maps are compared with our first order model for preferential evaporation based on ab initio calculations. The justification for making such comparisons is based on the fact that we are comparing changes in the ion evaporation maps associated with small but relatively homogenous regions of the microstructure. In these small regions, the effects of structure and chemistry can be effectively normalized with respect to all the other diverse array of parameters affecting the detection of multiple hits (eg. specimen geometry, trajectory aberrations, etc.). We see this study as a first step in linking atomistic scale modeling to experimental observations based on ion evaporation maps and hence develop a stronger mechanistic understanding and interpretation of preferential evaporation in atom probe tomography.

This work develops an atomistic modeling strategy to quantify the contributions of materials chemistry and structure to image resolution in APT. In this paper, we consider the relationship between the critical evaporation field F_e and chemistry, and in particular the changes in F_e due to dimer evaporations. The quality of the atom probe results is dependent on the selection of reconstruction parameters, particularly F_{op}, which is closely related to the F_e value. By identifying the energetics of field evaporation via a first principles approach, the reconstruction parametrization is more accurate, particularly for dimer events, leading to improved image resolution in the atom probe.

The remainder of the paper is organized as follows. Sections 2.1 and 2.2 describe the background of the experimental and computational details used in this work. The acquisition of the field evaporation value, using simulation results and numerical analysis is described in Section 3, while Section 4 shows the comparison between evaporation maps acquired from experimental results with the ab initio data.

2. Background

2.1. Experimental details

The atom probe experiment was performed on an Al–3.65Mg–.0566Sc (atomic percent) alloy. The data was collected with LEAP-3000X atom probe in voltage mode, with a temperature of 50 K, flight length of 160 mm, and pressure of 5.6×1011 Torr. The sample had an FCC Al matrix with $L1_2$ Al–Sc precipitates. The data considered in this paper is limited to the precipitate phase, which is shown in Fig. 1. Both the equilibrium Al–Mg–Sc phase diagram [35] and first principles calculations [36] indicate no solubility of Mg in the $L1_2$-Al_3Sc phase, agreeing with our experimental results.

In this paper, to compare the evaporation fields of single ions and dimers from both first principles calculations and experiment, we employ the concept of an ion evaporation map. Ion evaporation maps describe how the ions evaporate from the

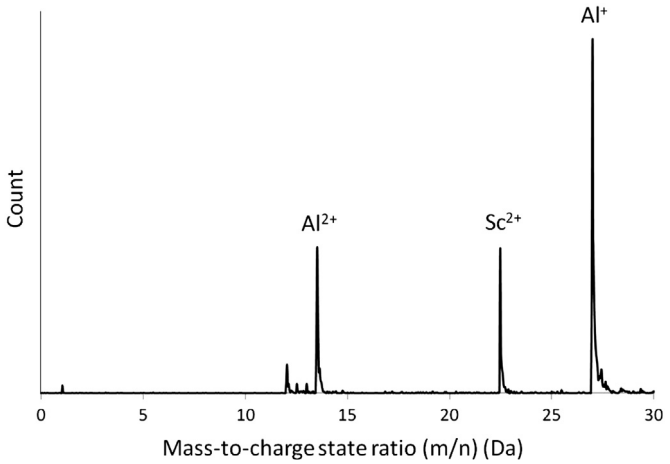

Fig. 1. The experimental data utilized in this paper. We limit the analysis and calculations to evaporation of Al and Sc atoms from an $L1_2$-Al_3Sc phase. Note: the number of Al^{2+} and Sc^{2+} ions evaporated from this precipitate is nearly equivalent, allowing us to use these two ions to compare with calculated results without considering relative quantities.

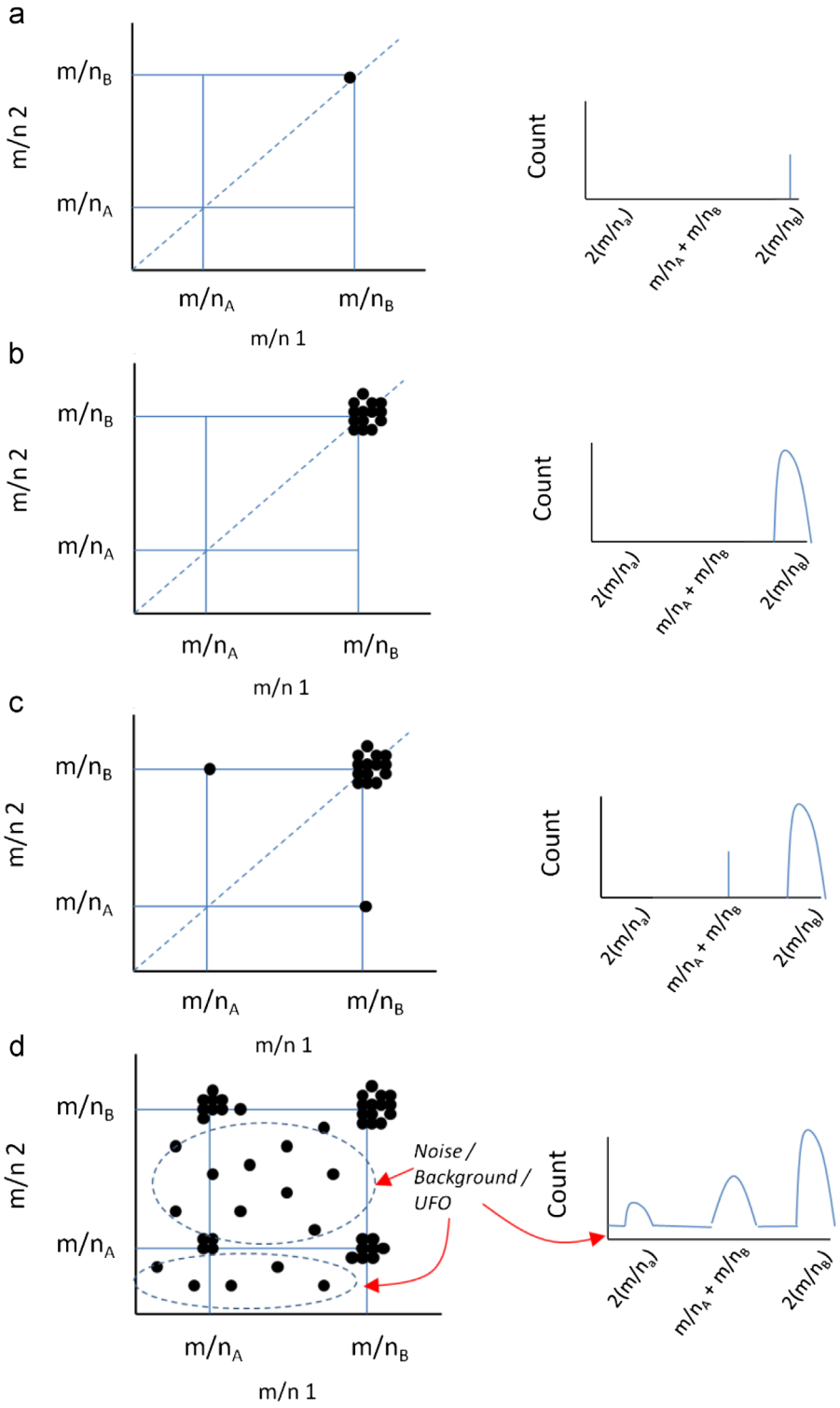

Fig. 2. Description of the population of an ion evaporation map. (a) One measurement of a dimer containing two *B* ions is plotted at $(m/n_B, m/n_B)$, with the count corresponding to one, although there are two overlapping points plotted in the evaporation map. (b) As additional dimers containing two *B* atoms is increased, the counts continue to increase. As typical mass spectra have peaks with width as opposed to a single vertical line, the points in the map do not all have same values, with the diameter of a circle defined by the points corresponding to the width of the spectral peak. (c) The addition of dimers containing dissimilar ions. In this case, the dimer count is one. Again there are two points plotted in the map, but in the case of dissimilar ions in the dimer, the two points are not overlapping. (d) A fully populated ion evaporation map. The counts correspond with the number of points for each dimer combination. The relationship in noise and background between the ion evaporation map and the *m*/*n* spectra is also shown.

surface. The axes of the maps are the mass-to-charge-state ratio *m*/*n* of one of the ions versus the *m*/*n* of the other ion. The map has a symmetry across the $x=y$ line, and for each dimer there are two points plotted in the ion evaporation map. These maps describe the likelihood and thereby relative evaporation fields of the different dimers. Fig. 2 describes the process for populating these maps, as compared to the *m*/*n* spectra.

The number of points within some radius of the dimer composition corresponds to the number of counts. As illustrated in Fig. 3, each point represented in an ion evaporation map indicates increased

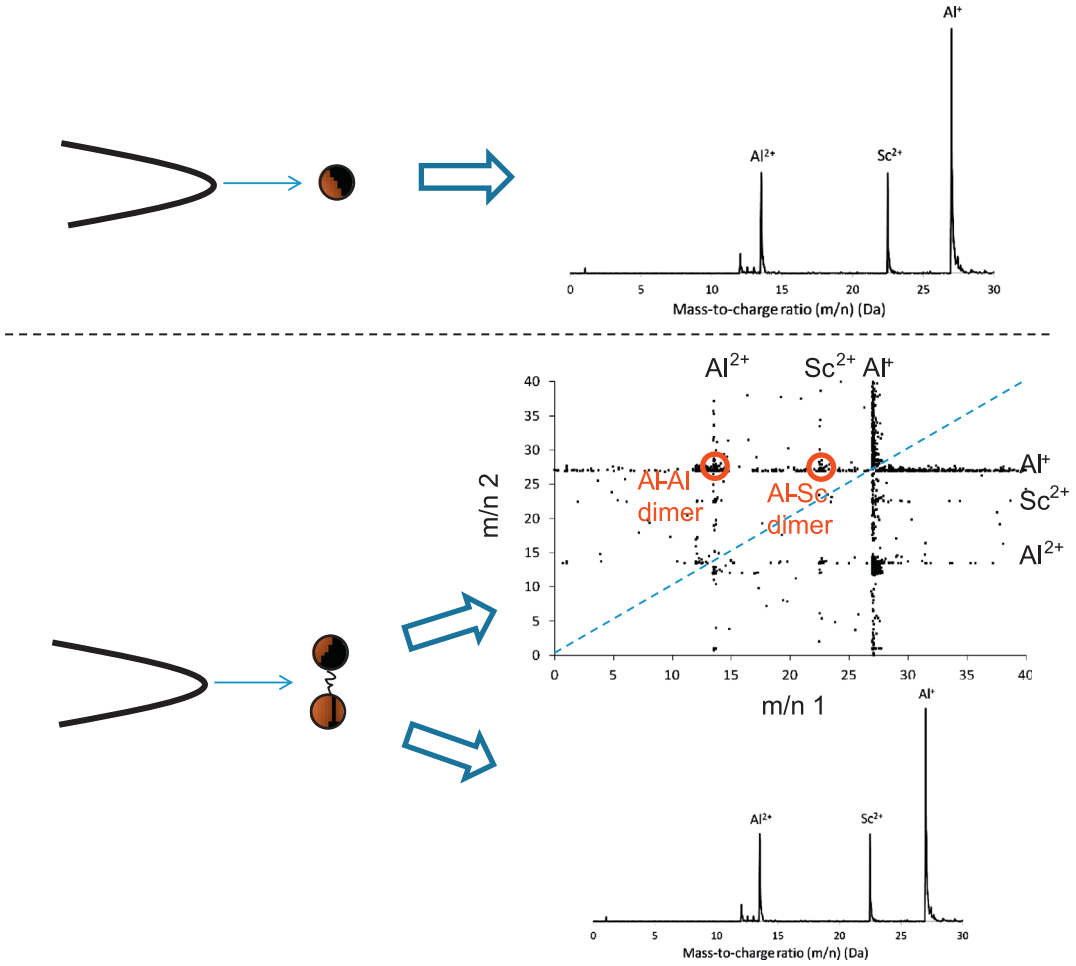

Fig. 3. Each single ion evaporation contributes only to the m/n spectrum, while each dimer evaporation contributes to both the m/n spectrum and the ion evaporation map. As the counts of Al^{2+} and Sc^{2+} are nearly equivalent, the relative evaporation fields of Al ions, Sc ions, Al–Al dimers and Al–Sc dimers can be extracted from the ion evaporation map. This experimental measurement of relative evaporation fields is described in Section 4.

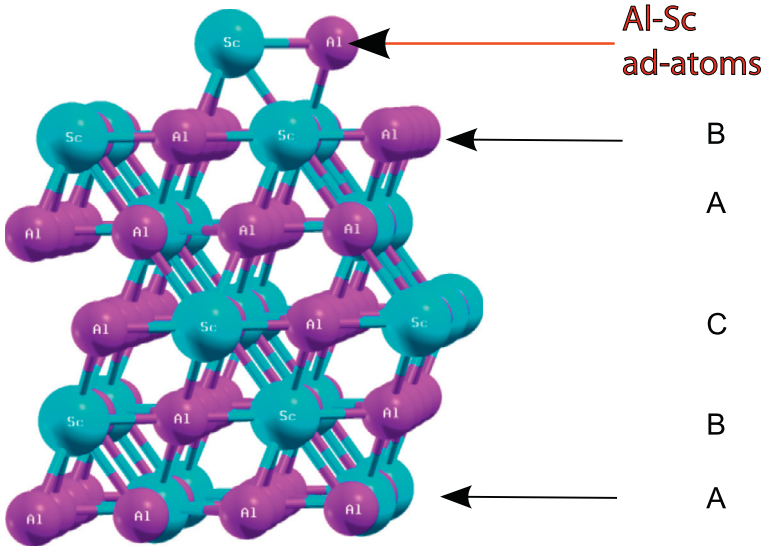

Fig. 4. Slab of Al_3Sc with Al–Sc ad-atoms on the surface, in an *A–B–C* layer scheme. The purple atoms (online) correspond to aluminum atoms and the blue (online) are the scandium atoms. The cell parameter used was 4.08 Å. (For interpretation of the references to color in this figure caption, the reader is referred to the web version of this article.)

likelihood of a dimer evaporation, and further means a lowering of the evaporation field relative to single ion evaporations. The ion evaporation map should be considered in conjunction with the m/n spectrum, as the m/n spectrum contains information on both single ion and dimer evaporations. However, in this case the counts of Al^{2+} and Sc^{2+} are nearly identical, and therefore if we limit our analysis to these two ions, we do not have to consider the m/n spectrum further. For this reason, if the number of points in Fig. 3 within the circle

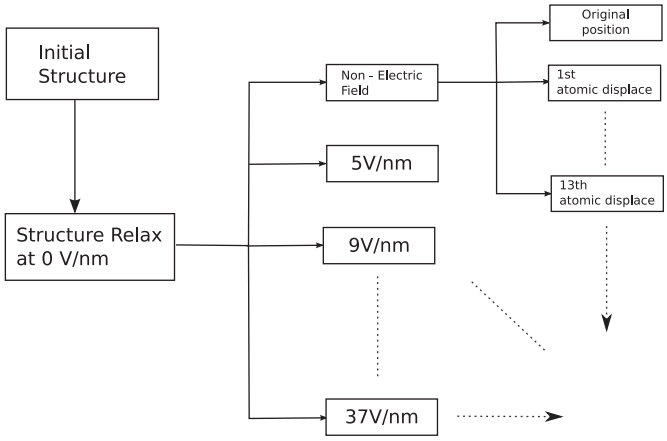

Fig. 5. This figure shows the procedure for each system configuration. After structure relaxation, different electric fields and distances for each ad-atom(s) configuration were used.

labeled Al–Sc dimer is less than the number of points within the Al–Al dimer circle, then we can say that the evaporation field of Al–Sc is greater than that of Al–Al, relative to the F_e of the constituent single ions because Al–Al evaporates as a dimer more easily than Al–Sc. As dimer evaporations contribute to both the m/n spectrum and the ion evaporation map, a greater number of dimers containing Al^{2+} ($m/n_1 = 13.5$, $m/n_2 =$ any value) implies fewer single ion evaporations. Therefore, the more points in the ion evaporation map with $m/n_1 \approx 13.5$ indicates reduced dimer evaporation field relative to single ion evaporation. The same analysis applies for Sc^{2+} dimer evaporations ($m/n_1 \approx 22.5$, $m/n_2 =$ any value). Further interpretation is provided in Section 4, where the relative evaporation fields of single ions and dimers are extracted from the ion evaporation map.

2.2. Computational details

The initial structure used for the simulation is composed of a slab of 80 atoms for Al_3Sc in the 111 direction along the z-axis.

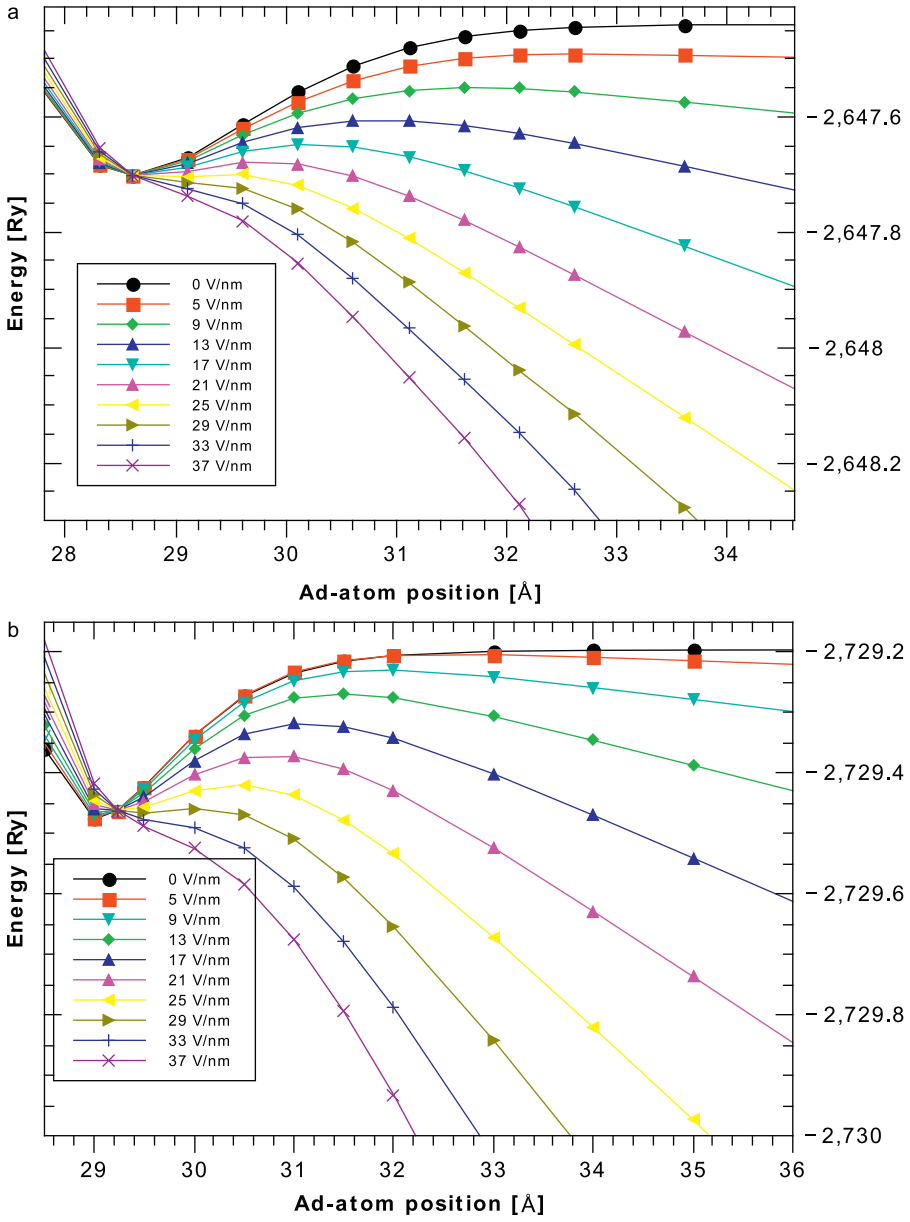

Fig. 6. Energy of the system as a function of a single ad-atom displacement. The evaporation field is defined as the electric field which corresponds with no hump. (a) Al atom on the surface. (b) Sc atom on the surface.

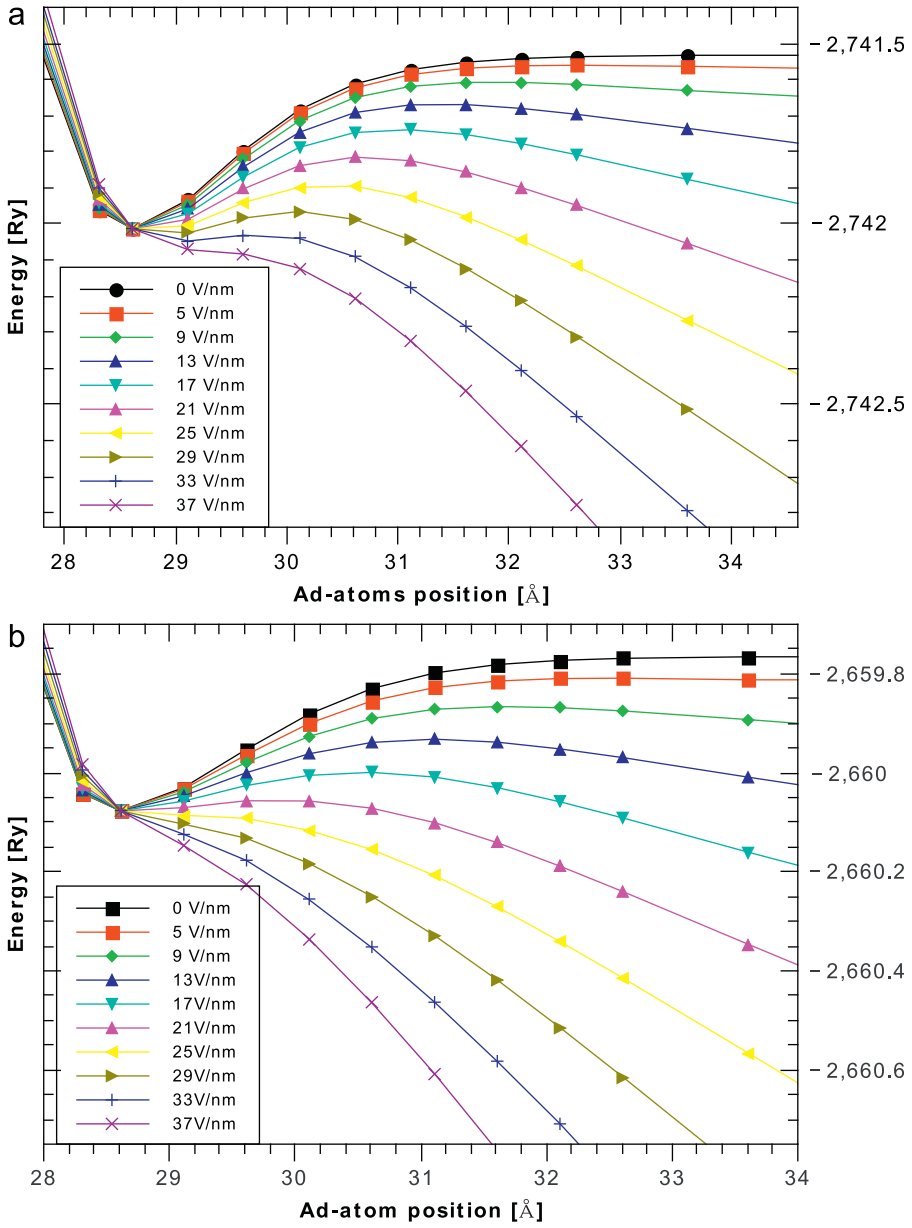

Fig. 7. Energy of the system as a function of the ad-atom dimer displacement. As for the single ad-atom case, the evaporation field corresponds with the evaporation field at which there is no hump. (a) Sc–Al atoms on the surface. (b) Al–Al atoms on the surface.

The slab is located in the middle of a supercell with a vacuum region of 15 Å to the borders of the supercell in the *z*-direction. The *x* and *y* size are five times the cell parameter for Al_3Sc (calculated after a relaxation procedure as 4.108 Å, agreeing with experiments [37]). The five planes that comprise the Al_3Sc surface are ordered in a layers scheme, as we can see in Fig. 4, with an Al–Sc dimer shown on the surface. Calculations were performed for four different configurations of ad-atoms on the surface: Al, Sc, Al–Al and Al–Sc. These have been considered in an initial position of the layer *C* of the structure, with only first neighbors used for the dimers (first neighbor distances are 2.9062 Å and 2.9086 Å for Al–Sc and Al–Al respectively).

The calculations in this work were performed using the Quantum-ESPRESSO code [38] (QE), under generalized gradient approximation (GGA) of density functional theory (DFT). The Al and Sc atoms were represented by the Vanderbilt ultra-soft pseudopotential scheme [39]. The energy cutoff chosen was 20 Ry, and a density cutoff of 200 Ry was used. The Marzari–Vanderbilt [40] scheme was used for the simulations. The electric field was incorporated as an additional term in the Hamiltonian and was applied to all simulations using the dipole correction [41] that is implemented in the QE package. The advantage of this method is that it avoids problems generated by the periodicity of the system in the *z*-axis with the vacuum space.

All the structures were relaxed using an ionic relaxation process. All the ionic relaxations were realized using the bfgs quasi-Newton based on the trust radius procedure without considering cell variation of the structure. The convergence criteria were set under the condition that atomic forces on every atom are lower than 1.0×10^{-3} (in atomic units) for all directions. There was no relaxation procedure for the structure under the presence of electric field, motivated by the similar behavior to the results presented in Ref. [8] and the computational time necessary when an electric field is incorporated.[1]

[1] The computational time using electric field in an ab initio simulation is frequently around 8 times than the same without an electric field, and highly

3. First principles calculated field evaporation

For each atomic configuration, the simulation procedure consisted of three principal parts: (1) an ionic relaxation of the surface with the ad-atom(s), without an Electric Field ($\vec{E}_F = 0$), (2) applying 10 different electric fields, between 0 and 37 V/nm, and (3) for each electric field applied, the ad-atom(s) on the surfaces were displaced to 13 different distances from their equilibrium position. A detailed description of the procedure is shown in Fig. 5.

In order to determine the field evaporation associated with each atomic configuration, the total energy of the system was calculated. These energies were obtained as a function of different electric fields and the distance between atoms of interest and the surface. Figs. 6 and 7 show the calculated results for the single ions and dimers, respectively.

Fig. 6 shows the variation of the energy of the system with ad-atom displacement from the surface for the case of Sc and Al ad-atom. A similar representation of the process is shown in Fig. 7 for the case of Al–Al and Al–Sc dimers. The displacement in the dimer case is for both atoms simultaneously. For all cases, as the electric field is increased the hump is reduced. The evaporation field is the electric field value at which the hump practically disappears, and is different for each type of ad-atom(s) on the Al_3Sc surface.

In order to determine the hump for each energy vs ad-atom position curve, we fit the results numerically with a standard seven parameter equation of the form [8]

$$E(z) = (a + bz + cz^2 + dz^3)\exp(-fz) + g + hz \tag{4}$$

where a, b, c, d, f, g and h are parameters to be determined numerically. Based on the numerical results from Eq. (4), we determine the position and the value of the hump of the curves in Figs. 6 and 7.

The activation energy (hump height) variation has been defined as the difference in energy between the maximum and minimum of each curve as shown in Fig. 8. For the case without electric field, the activation energy corresponds to the value between the minimum and the asymptote reached. We define the critical evaporation field as the electric field where the activation energy is equal to zero. The hump height variation for each curve in Figs. 6 and 7 are plotted in Fig. 9. While Eq. (3) suggests that these curves should have a square root dependency, our results show a different pattern, although this pattern agrees with previous evidence [30,8,42]. In order to determine an accurate value of F_e, an additional approximation is utilized in Fig. 9. The hump variation follows a sigmoid function, and therefore to fit a line to this curve we use a generalized logistic function (or Richard's curve) given by

$$H[F] = Q = a + \frac{k-a}{(1 + q * \exp[-b * (F-m)])^{(1/n)}} \tag{5}$$

where H corresponds to the activation energy, F is the electric field, and the parameters a, b, k, q, m and n are determined numerically. The position where the fitted curve of Eq. (5) has zero value corresponds to the evaporation field that we determine for the different kinds of ad-atom(s) on the Al_3Sc surface. The curves of the four different configurations with the fit are shown in Fig. 9.

The values of the field evaporation for each configuration are 24.85 V/nm, 28.99 V/nm, 32.03 V/nm and 36.33 V/nm for Al–Al, Al, Sc and Al–Sc ad-atom(s), respectively. It is important to highlight that the value associated to a single Al atom ($\sim$29 V/nm) is substantially different of the reported for single Al atom in a Al(111) surface. This result suggests a high dependence of the surface, in our case the surface Al_3Sc (111), and the critical evaporation field.

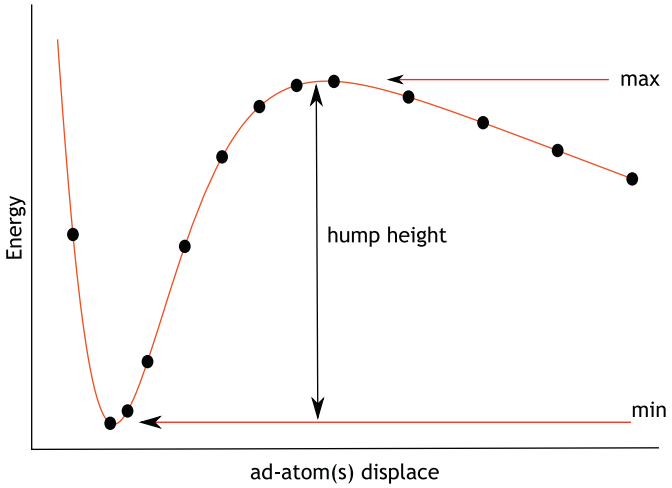

Fig. 8. Schematic definition of the activation energy. The maximum and minimum values are determined numerically.

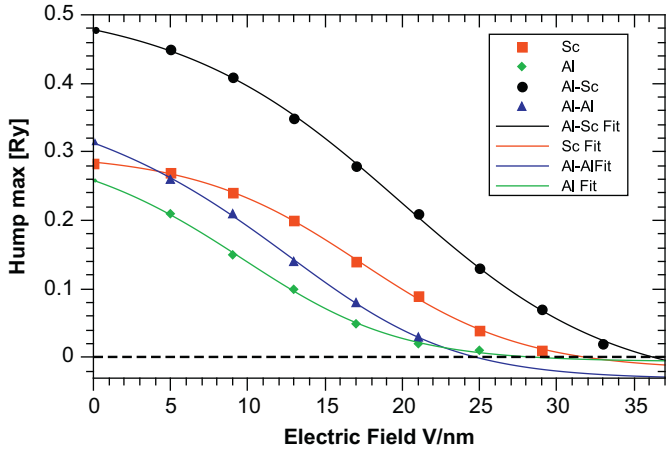

Fig. 9. The activation energy from the simulations shown in Figs. 6 and 7. The dashed black line corresponds to the zero value of the activation energy. The evaporation field is defined by the intersection of the fitted curves with zero activation energy. The values of F_e in V/nm are calculated as: 24.85 for Al–Al dimer, 28.99 for Al ion, 32.03 for Sc ion, and 36.33 for Al–Sc dimer.

4. Discussion

Having developed the energetics of different evaporation events, the experimental data was analyzed for comparison between the calculation and experiment. To convert the experimental data into a form that describes dimer formation, the multi-ion hits were plotted in the form of an ion evaporation map (Fig. 10), where each point represents a multi-hit event. As previously discussed, the majority of points are not directly due to dimers, but the relative differences between chemistries is representative of a relative change in dimer counts. In the ion evaporation map, the mass-to-charge state ratio (m/n) of one of the ions is plotted against the m/n of the other ion. The ion

(*footnote continued*)
dependent on the value and the initial charge density. Vacuum space and cell size are important factors as well.

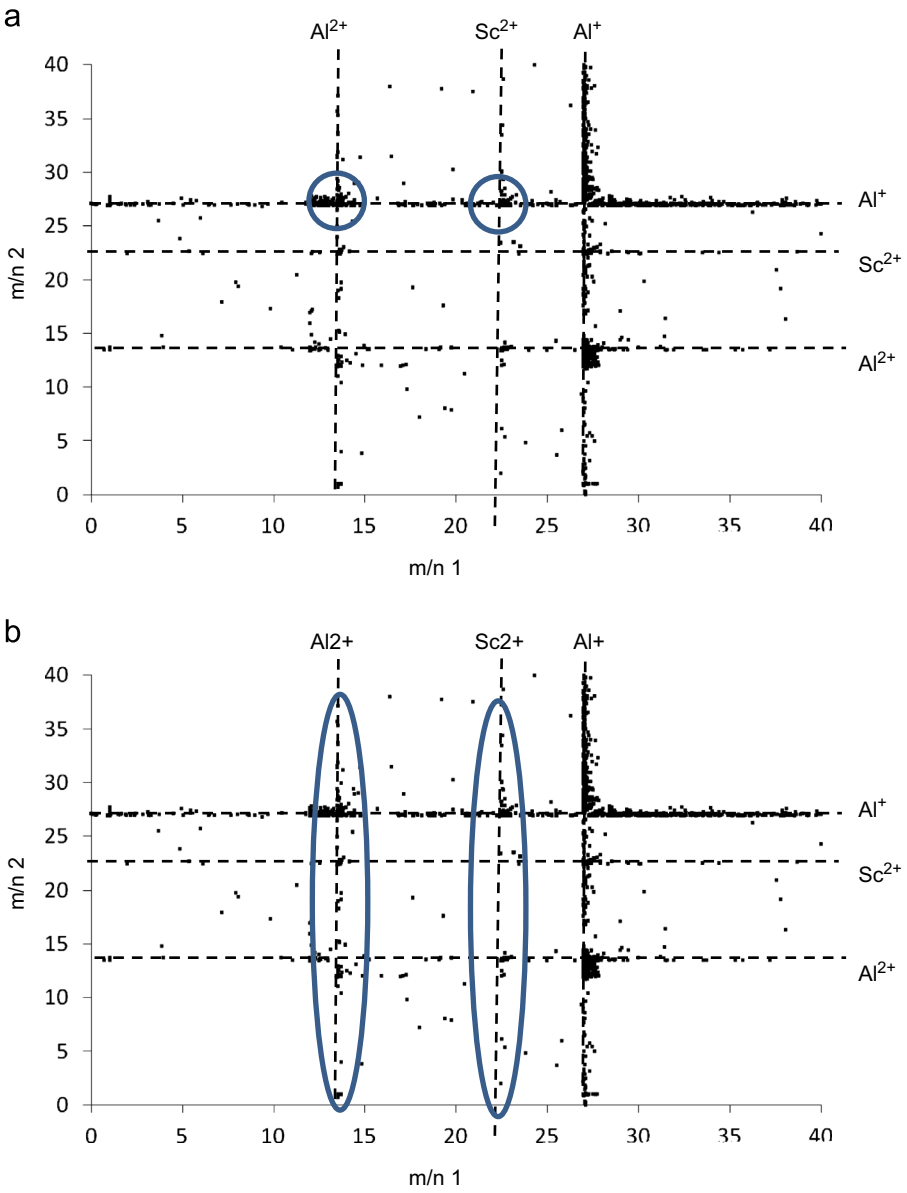

Fig. 10. Ion evaporation map for Al_3Sc phase. This figure plots dimer chemistries, where each dimer comprises of (m/n 1, m/n 2). (a) The number of Al^{2+}–Al^{+} dimers is greater than the number of Sc^{2+}–Al^{+} dimers, although there are equivalent amounts of Sc^{2+} and Al^{2+} in the phase. This result indicates that Al–Al has a lower F_e than Al–Sc. (b) The number of dimers containing Al^{2+} is greater than the dimers with Sc^{2+}. This result means that the F_e(Al–Sc) minus F_e(Sc) is greater than F_e(Al–Al) minus F_e(Al).

evaporation map includes only the ions that were in the precipitate phase because the calculations were done for the Al_3Sc structure. For this reason, very little Mg is seen in the figure, as it has limited solubility in Al_3Sc [35,36]. The primary three ions present are Al^{2+} (m/n 13.5 Da), Sc^{2+} (m/n 22.5 Da), and Al^{+} (m/n 27.0 Da). The number of ions which evaporated as Al^{2+} in the overall sample is approximately equivalent to the number of Sc^{2+} ions. In the precipitate, the number of Sc^{2+} evaporations was significantly greater than the number of ions evaporated as Al^{2+}. We use these ions as our standard of comparison in this section. It is important to note that based on the DFT methodology, no polarization of core electrons in the external field is allowed. This is unavoidable within the pseudopotential framework, although it could be done within an all-electron treatment [43].

In Fig. 10(a), the circled regions indicate relative quantities of Al–Al dimer and Al–Sc dimer. A third dimension showing counts could be added to the figure, but for reasons of clarity, only two dimensions are included. The number of Al^{2+}–Al^{+} dimers shown in the ion evaporation map is greater than the number of Al^{+}–Sc^{2+} dimers. Since the amount of Al^{2+} is less than Sc^{2+} in the precipitate phase, we conclude that the Al–Al dimer is much more likely to form than the Al–Sc dimer. Further, the Sc–Sc dimer is unlikely to form as very few cases appear in this map. These experimental results show that Al–Al dimer has a lower evaporation field than the Al–Sc dimer. This experimental measurement agrees with our calculations.

To compare the relationship between evaporation fields of dimers versus constituent atoms, the regions circled in Fig. 10(b) were considered. Again we see more dimers within the Al^{2+} than in the Sc^{2+} region. Given that the total number of Al^{2+} ions in the Al_3Sc phase is equivalent to the number of Sc^{2+} ions, we identify that the ratio of dimer/ion for Al^{2+} is much greater than the ratio of dimer/ion for Sc^{2+}. From this result, we

conclude that the ratio of F_e(dimer)/F_e(single ion) is less for Al than for Sc. This experimental conclusion also agrees with our calculations, which calculated that F_e(Al–Al) is less than F_e(Al), while the F_e(Sc) was calculated as less than F_e(Al–Sc).

We have demonstrated in this section the use of ion evaporation maps to describe relative evaporation fields of different ions/dimers. These experimental results were in agreement with the first principles calculations, validating the mechanism of evaporation that was modeled.

5. Conclusions

In this paper, ab initio techniques have been used to more fully describe the evaporation procedure. The way that atoms are evaporated from the surface (single ions, dimers, and more complex arrangements) is a fundamental problem in atom probe tomography with implications for reconstruction accuracy. A detailed description of the evaporation process on an Al_3Sc surface has been compiled, with the calculated field evaporation values for single ions and dimers qualitatively agreeing with atom probe experimental measurements. The results rank the evaporation fields in increasing difficulty of evaporation from Al_3Sc structure as: Al–Al dimer, Al ion, Sc ion, and Al–Sc dimer. The implication of this work for improved image resolution in the atom probe was discussed, with the modeled mechanism agreeing with experimental results and providing improved physical description of the evaporation process.

Acknowledgments

This work was supported by NSF-CDI Type II program: Grant #PHY 09-41576; NSF-ARI Program: CMMI 09-3890182; the Defense Advanced Research Projects Agency (DARPA) N/MEMS S&T Fundamentals program under Grant no. N66001-10-1-4004 issued by the Space and Naval Warfare Systems Center Pacific (SPAWAR), and Air Force Office of Scientific Research (AFOSR) Grant no. FA9550-10-1-0256, FA9550-11-1-0158 and FA9550-12-0496. J.P. acknowledges CONICYT, Becas-Chile postdoctoral Chilean grant. K.R. acknowledges support from the Wilkinson Professorship of Interdisciplinary Engineering.

References

[1] D. Blavette, B. Deconihout, S. Chambreland, A. Bostel, Three-dimensional imaging of chemical order with the tomographic atom-probe, Ultramicroscopy 70 (3) (1998) 115–124.
[2] M.K. Miller, R.G. Forbes, Atom probe tomography, Materials Characterization 60 (2009) 461–469.
[3] M.K. Miller, E.A. Kenik, Atom probe tomography: a technique for nanoscale characterization, Microscopy and Microanalysis 10 (3) (2004) 336–341.
[4] E.R. McMullen, J.P. Perdew, Effects of an intense electric field on metal surface geometry, Solid State Communications 44 (6) (1982) 945–949.
[5] E.R. McMullen, J.P. Perdew, Theory of field evaporation of the surface layer in jellium and other metals, Physical Review B 36 (5) (1987) 2598–2606.
[6] H.J. Kreuzer, Self-consistent calculation of atomic adsorption on metals in high electric fields, Physical Review B 45 (20) (1992) 12050–12055.
[7] J. Neugebauer, M. Scheffler, Theory of adsorption and desorption in high electric fields, Surface Science 287 (1993) 572–576.
[8] C.G. Sánchez, A.Y. Lozovoi, A. Alavi, Field-evaporation from first-principles, Molecular Physics 102 (2004) 1045–1055.
[9] T. Ono, T. Sasaki, J. Otsuka, K. Hirose, First-principles study on field evaporation of surface atoms from W(011) and Mo(011) surfaces, Surface Science 577 (2005) 42–46.
[10] F. Vurpillot, S. Bostel, D. Blavette, A new approach to the interpretation of atom probe field-ion microscopy images, Ultramicroscopy 89 (1) (2001) 137–144.
[11] C. Oberdorfer, G. Schmitz, On the field evaporation behavior of dielectric materials in three-dimensional atom probe: a numeric simulation, Microscopy and Microanalysis 17 (2011) 15–25.
[12] E.A. Marquis, B.P. Geiser, T.J. Prosa, D.J. Larson, Evolution of tip shape during field evaporation of complex multilayer structures, Journal of Microscopy 241 (3) (2011) 225–233.
[13] B.P. Geiser, D.J. Larson, E. Oltman, S. Gerstl, D. Reinhard, T.F. Kelly, T.J. Prosa, Wide-field-of-view atom probe reconstruction, Microscopy and Microanalysis 15 (2) (2009) 292–293.
[14] T. Boll, T. Al-Kassab, Interpretation of atom probe tomography data for the intermetallic tial+nb by means of field evaporation simulation, Ultramicroscopy 124 (2013) 1–5.
[15] P.A. Ignatiev, V.S. Stepanyuk, Effect of the external electric field on surface states: an ab initio study, Physical review B 84 (7) (2011) 7.
[16] B. Gault, F.D. Geuser, L.T. Stephenson, M.P. Moody, B.C. Muddle, S.P. Ringer, Estimation of the reconstruction parameters for atom probe tomography, Microscopy and Microanalysis 14 (4) (2008) 296–305.
[17] B. Gault, D. Haley, F.D. Geuser, M.P. Moody, E.A. Marquis, D.J. Larson, B.P. Geiser, Advances in the reconstruction of atom probe tomography data, Ultramicroscopy 111 (6) (2010) 448–457.
[18] F.D. Geuser, W. Lefebvre, F. Danoix, F. Vurpillot, B. Forbord, D. Blavette, An improved reconstruction procedure for the correction of local magnification effects in three-dimensional atom-probe, Surface and Interface Analysis 601 (2) (2007) 268–272.
[19] F. Vurpillot, M. Gruber, G.D. Costa, I. Martin, L. Renaud, A. Bostel, Pragmatic reconstruction methods in atom probe tomography, Ultramicroscopy 111 (8) (2011) 1286–1294.
[20] B. Gault, S.T. Loi, V.J. Araullo-Peters, L.T. Stephenson, M.P. Moody, S.L. Shrestha, R.K.W. Marceau, L. Yao, J.M. Cairney, S.P. Ringer, Dynamic reconstruction for atom probe tomography, Ultramicroscopy 111 (11) (2011) 1619–1624.
[21] P. Bas, A general protocol for the reconstruction of 3d atom probe data, Applied Surface Science 87 (88) (1995) 298–304.
[22] T.T. Tsong, Field ion image formation, Surface Science 70 (1) (1978) 211–233.
[23] T. Ono, K. Hirose, First-principles study on field evaporation for silicon atom on Si(001) surface, Journal of Applied Physics 95 (3) (2004) 1568–1571.
[24] F. Tang, B. Gault, S. Ringer, J.M. Cairney, Optimization of pulsed laser atom probe (plap) for the analysis of nanocomposite Ti–Si–N films, Ultramicroscopy 110 (7) (2010) 836–843.
[25] B. Gault, E.A. Marquis, D.W. Saxey, G.M. Huges, D. Mangelinck, E.S. Toberer, G.J. Snyder, High-resolution nanostructural investigation of Zn_4Sb_3 alloys, Scripta Materiala 63 (2010) 784–787.
[26] O. Jagutzki, A. Cerezo, A. Czasch, R. Dörner, M. Hattab, M. Huang, W. Mergel, U. Spillmann, K. Ullmann-Pfleger, T. Weber, H. Schmidt-Böcking, G.D.W. Smith, Multiple hit readout of a microchannel plate detector with a three layer delay-line anode, IEEE Transactions on Nuclear Science 49 (5) (2002) 2477–2483.
[27] G.D. Costa, F. Vurpillot, A. Bostel, M. Bouet, B. Deconihout, Design of a delay-line position-sensitive detector with improved performance, Review of Scientific Instruments 76 (2005) 013304.
[28] R. Gomer, Field-emission, field-ionization and field desorption, Surface Science 1 (3) (1994) 129–152.
[29] R.G. Forbes, Field evaporation theory: a review of basic ideas, Applied Surface Science 87 (1995) 1–11.
[30] R.G. Forbes, R.K. Biswas, K. Chibane, Field evaporation theory: a re-analysis of published field sensitivity data, Surface Science 114 (2) (1982) 498–514.
[31] R. Gomer, L.W. Swanson, Theory of field desorption, Journal of Chemical Physics 38 (7) (1963) 1613–1629.
[32] N.M. Miskovsky, T.T. Tsong, Field evaporation of gold in single- and double-electrode systems, Physical Review B 46 (4) (1992) 2640–2643.
[33] F.D. Geuser, B. Gault, A. Bostel, F. Vurpillot, Correlated field evaporation as seen by atom probe tomography, Surface Science 601 (2) (2007) 536–543.
[34] D.W. Saxey, Correlated ion analysis and the interpretation of atom probe mass spectra, Ultramicroscopy 111 (6) (2011) 473–479.
[35] J. Grobner, R. Schmid-Fetzer, A. Pisch, G. Cacciamani, P. Riani, N. Parodi, G. Borzone, A. Saccone, R. Ferro, Experimental investigations and thermodynamic calculation in the Al–Mg–Sc system, Zeitschrift fur Metallkunde 90 (11) (1999) 872–880.
[36] E.A. Marquis, D.N. Seidman, M. Asta, C. Woodward, Composition evolution of nanoscale Al_3Sc precipitates in an Al–Mg–Sc alloy: experiments and computations, Acta Materialia 54 (1) (2006) 119–130.
[37] Y. Harada, D.C. Hunand, Microstructure of Al3Sc with ternary transition–metal additions, Materials Science and Engineering A—Structural Materials Properties Microstructure and Processing 329 (2002) 686–695.
[38] P. Giannozzi, S. Baroni, N. Bonini, M. Calandra, R. Car, C. Cavazzoni, D. Ceresoli, G.L. Chiarotti, M. Cococcioni, I. Dabo, A.D. Corso, S. Fabris, G. Fratesi, S. de Gironcoli, R. Gebauer, U. Gerstmann, C. Gougoussis, A. Kokalj, M. Lazzeri, L. Martin-Samos, N. Marzari, F. Mauri, R. Mazzarello, S. Paolini, A. Pasquarello, L. Paulatto, C. Sbraccia, S. Scandolo, G. Sclauzero, A.P. Seitsonen, A. Smogunov, P. Umari, R.M. Wentzcovitch, Quantum espresso: a modular and open-source software project for quantum simulations of materials, Journal of Physics: Condensed Matter 21 (39) (2009) 395502. (19 pp).
[39] F. authors refer to the website. We use the pseudopotentials Al.pbe-n-van.upf and Sc.pbe-nsp-van.upf from 〈http://www.quantum-espresso.org〉, 〈http://www.quantum-espresso.org〉, 2011.
[40] N. Marzari, D. Vanderbilt, M. Payne, Ensemble density-functional theory for *Ab Initio* molecular dynamics of metals and finite-temperature insulators, Physical Review Letters 79 (7) (1997) 1337–1340.
[41] L. Bengsston, Dipole correction for surface supercell calculations, Physical Review B 59 (19) (1999) 12301–12304.
[42] C.G. Sánchez, A.Y. Lozovoi, Field evaporation of adatoms from metal surfaces, personal communication.
[43] N.D. Lang, Bias-induced transfer of an aluminum atom in the scanning tunneling microscope, Physical Review B 49 (3) (1994) 2067–2071.